Multispectral LEDs Eliminate Lipofuscin-Associated Autofluorescence for Immunohistochemistry and CD44 Variant Detection by in Situ Hybridization in Aging Human, non-Human Primate, and Murine Brain

Philip A. Adeniyi[1] [ID], Katie-Anne Fopiano[2], Fatima Banine[3], Mariel Garcia[1], Xi Gong[1], C. Dirk Keene[4], Larry S. Sherman[3], Zsolt Bagi[2] and Stephen A. Back[1,5]

Abstract

A major limitation of mechanistic studies in aging brains is the lack of routine methods to robustly visualize and discriminate the cellular distribution of tissue antigens using fluorescent immunohistochemical multi-labeling techniques. Although such approaches are routine in non-aging brains, they are not consistently feasible in the aging brain due to the progressive accumulation of autofluorescent pigments, particularly lipofuscin, which strongly excite and emit over a broad spectral range. Consequently, aging research has relied upon colorimetric antibody techniques, where discrimination of tissue antigens is often challenging. We report the application of a simple, reproducible, and affordable protocol using multispectral light-emitting diodes (mLEDs) exposure for the reduction/elimination of lipofuscin autofluorescence (LAF) in aging brain tissue from humans, non-human primates, and mice. The mLEDs lamp has a broad spectral range that spans from the UV to infrared range and includes spectra in the violet/blue and orange/red. After photo quenching, the LAF level was markedly reduced when the tissue background fluorescence before and after mLEDs exposure was compared (p < 0.0001) across the spectral range. LAF elimination was estimated at $95 \pm 1\%$. This approach permitted robust specific fluorescent immunohistochemical co-visualization of commonly studied antigens in aging brains. We also successfully applied this method to specifically visualize CD44 variant expression in aging human cerebral white matter using RNAscope fluorescent in-situ hybridization. Photo quenching provides an attractive means to accelerate progress in aging research by increasing the number of molecules that can be topologically discriminated by fluorescence detection in brain tissue from normative or pathological aging.

[1]Departments of Pediatrics, Oregon Health & Science University, Portland, Oregon
[2]Department of Physiology, Medical College of Georgia, Augusta University, Augusta, GA, USA
[3]Division of Neuroscience, Oregon National Primate Research Center, Oregon Health and Science University, Beaverton, OR, USA
[4]Department of Laboratory Medicine and Pathology, University of Washington, Seattle, Washington, USA
[5]Departments of Neurology, Oregon Health and Science University, Portland, Oregon

Katie-Anne Fopiano, Fatima Banine, These authors contributed equally to this study.

Corresponding Authors:
Philip A. Adeniyi, PhD, Department of Pediatrics, Oregon Health & Science University, Mail-Code L481, 3181 S.W. Sam Jackson Park Rd. Portland, Oregon 97239–3098, USA.
Email: adeniyi@ohsu.edu

Stephen A. Back, MD, PhD, Department of Pediatrics and Neurology, Oregon Health & Science University, Mail-Code L481, 3181 S.W. Sam Jackson Park Rd. Portland, Oregon 97239–3098, USA.
Email: backs@ohsu.edu

Introduction

Although fluorescence microscopy is widely used in neuroanatomical and neuropathological studies, its application in aging research has been hampered by the progressive accumulation of autofluorescent pigments including lipofuscin in the aging brain (Terman and Brunk, 2004a; Moreno-García et al., 2018). Lipofuscin is a non-degradable intralysosomal, brown-yellow, electron-dense, polymeric autofluorescent substance that has been reported to accumulate progressively over time in lysosomes of postmitotic cells, including cardiac myocytes (Terman and Brunk, 2004b), retinal cells (Andrews and Brizzee, 1986), and neurons (Brizzee et al., 1969). Lipofuscin is not the only endogenous substance that results in autofluorescence in mammalian tissues. Collagen, elastin, flavins, and hemosiderin are also problematic naturally fluorescent extracellular matrix components in mammalian tissues (Banerjee et al., 1999; Schnell et al., 1999; Viegas et al., 2007). In addition, red blood cells and macrophages have also been recognized as a major source of autofluorescence or high background in unfixed or poorly fixed tissue samples (Whittington and Wray, 2017). Despite several decades of research, the application of fluorescence multi-labeling immunohistochemistry (IHC) to the aging brain has been hampered by limited progress to quench the endogenous tissue autofluorescence of lipofuscin and other compounds that are highly enriched in aging primates and rodents (Brizzee and Johnson, 1970; Schnell et al., 1999).

The emission spectrum of lipofuscin overlaps with that of commonly used fluorophores, which makes it extremely difficult to distinguish between lipofuscin-associated autofluorescence (LAF) and specific IHC-associated fluorophores in aged human neural tissues (Corrêa et al., 1980; Santer et al., 1980). Lipofuscin accumulates in the cytoplasm of neural cells in an age-dependent manner where it mimics the appearance of all known fluorophores used in IHC due to its broad emission spectrum, which includes emission ranges from blue to red. LAF also accumulates in non-human primates, such as macaque monkeys, as well as rabbits, cats, rats, and mice (Brizzee and Johnson, 1970; Andrews and Brizzee, 1986; Schnell et al., 1999; Duong and Han, 2013). Lipofuscin poses the greatest challenge because it localizes within the cytoplasm of postmitotic cells. By contrast, blood vessel-associated autofluorescence (BAF) can be easily

identified as artifactual (Banerjee et al., 1999; Schnell et al., 1999; Viegas et al., 2007). Moreover, the red blood cell autofluorescence can be eliminated/reduced by immersion in hydrogen peroxide.

There have been several attempts to release or eliminate the autofluorescence of lipofuscin from aged brain sections with partial success. Consequently, there has been a reliance on colorimetric stains visualized using immunohistochemistry combined with Nissl or hematoxylin and eosin, which has been challenging for the detection of two or more antigens. Previous attempts to reduce or eliminate the LAF from samples employed several non-chemical approaches such as the use of a customized filter set (Pang et al., 2013), Autofluorescence Identifier (Baharlou et al., 2021), non-negative matrix factorization (Woolfe et al., 2011) and hyperspectral analysis of fluorophores (Leavesley et al., 2012). Given the limited success with these approaches, other laboratories employed chemical treatments to reduce LAF. However, they were also only partially effective and, in some instances, also reduced specific staining (Duong and Han, 2013). These chemical treatments included $CuSO_4$, $CuCl_2$, Na_2SO_4, and Sudan Black (Schnell et al., 1999; Viegas et al., 2007). Although quenching of LAF with light-emitting diodes (LED) in several tissues was attempted, success was limited by the usage of light of low wattage, lack of optimal temperature control, or limitations in terms of the number of samples that could be analyzed at one time (Duong et al., 2013; Sun et al., 2017). Hence, there is a need for a rapid cost-effective method for near-complete elimination of LAF while maintaining the quality and integrity of the tissues to enhance reproducibility and provide reliable results. Here we determined if high-intensity multispectral light-emitting diodes (mLEDs) could be employed for photo quenching of tissue autofluorescence in an aging brain where high LAF obscures antigen detection by immunofluorescence histochemistry.

We also determined if mLED photo quenching can be generalized to other widely used fluorescent histological approaches. We employed mLED photo quenching to visualize the expression of CD44 variants using a RNAscope fluorescence in situ hybridization protocol. CD44 variants were detected in aging human cerebral white matter from subjects with confirmed vascular pathology and a history of vascular cognitive impairment and dementia (VCID). We focused on CD44 because we previously found that hyaluronan, a CD44 ligand, was enriched in frontal cerebral white matter lesions in cases with vascular dementia (Back et al., 2011). We report here the enrichment of multiple RNA splice variants of CD44 including variants encoded by CD44 variant exon 8 (v8) in white matter lesions visualized by RNAscope. Our protocol for the elimination of LAF tissue autofluorescence thus appears compatible with several commonly employed histological approaches. These technical advances may provide a novel means to accelerate progress in aging research by increasing the number of molecules

Table 1. Relative Fluorescence Values (Mean ± S.E.M) Acquired at 405, 488, and 561 nm Wavelength in Human, Monkey, and Mouse Frontal White Matter as Shown in figure 3.

Species	Blue (a.u.)	Green (a.u.)	Red (a.u.)
Mice	49.21 ± 5.55	45.64 ± 3.23	66.05 ± 2.43
Monkey	3082.16 ± 215.63	2693.23 ± 289.80	2051.45 ± 210.44
Human	3460.31 ± 97.73	2999.77 ± 108.89	2717.30 ± 95.38

that can be topologically discriminated in brain tissue from normative or pathological aging.

Materials and Methods

Ethics Statement, Subjects, and Tissue Handling

Written informed consent was obtained from all individual study participants. All procedures involving human subjects were approved by the University Institutional Review Board following the Helsinki Declaration of the World Medical Association. Details of the human (average age of 89.9 years) tissue samples studied are provided in supplementary table 1. Brain tissue from four Rhesus macaque (*Macaca mulatta*) was obtained from the Aging Primate Resource tissue bank of the Oregon National Primate Research Center and included tissue from one male (24 years old) and three females monkeys (7, 9, and 20 years old). Aging murine C57Bl6 brain tissue was from two animals (2.5 years old) and two controls (6 months old).

Tissue Preparation

All human, macaque, and murine brain tissue sections (30 or 50 μm) were fixed in 4% paraformaldehyde and sectioned free-floating using a vibratome or cryostat. Tissue sections for photo–quenching (PhotoQ) were immersed in 6-well plates (2 sections per well) filled to the brim with PBS and placed in the PhotoQ chamber (see figures 1 and Supplemental figure 1). The chamber held six 6-well plates and could be expanded as needed. Control samples were immersed in PBS under the same conditions but without PhotoQ.

Measurements and Quantification of Fluorescence Intensity

The reduction of fluorescence intensity (figures 2 to 4 and supplemental figure 3) was quantified in Fiji, a Java-based ImageJ analysis software (an open-source image program available from the National Institutes of Health (NIH)). We determined the fluorescence level of the PhotoQ-treated (i.e., light exposure) and non-PhotoQ (i.e., no light exposure) sections and tissue background before and after each treatment duration (t = 12, 24, or 72 h), see Supplemental Figures 1 and 2. The LAF level was quantitatively estimated with Image J by randomly drawing four separate lines (300 μm) on the micrograph using the Straight, freehand tool, as shown in supplemental figure 2. Fluorescence intensity values were generated as a histogram at 1 μm intervals along the 300 μm line using the Plot of Clipboard/ Plot Profile function. LAF level was determined by subtracting average background values (Background Gray Value (Δ_0)) from the average peak fluorescent intensity values (Gray Value of fluorescence (I_0), which corresponded to regions

on the photomicrograph where the line intersected with granular-appearing autofluorescent aggregates. This approach was selected so that blood vessel-associated autofluorescence was not included in the estimates of total LAF in the image. The calculation of LAF was done as follows:

[I]: Fluorescence Level = [Gray Value of fluorescence (I_0) – Background Gray Value (Δ_0)]

[II]: Fluorescence Level Reduction (%) = [100 – (($I_0 - \Delta_0$) – ($I_t - \Delta_t$))/ ($I_0 - \Delta_0$)]

Where I_0 and Δ_0 are the initial mean intensity values and tissue background values respectively (n = 4 ROIs per section; n = 4 quadruplicate images per subject), and I_t and Δ_t are the mean intensity values and tissue background after t (hr) of PhotoQ. The statistical significance was determined using two–way ANOVA analysis and Tukey's multiple mean comparisons of fluorescence level [I], percentage reduction for the treated duration [II], and LAF particle size.

Apparatus set-up and Protocol for Photo Quenching (PhotoQ)

A high output 87-watt LED array (catalog #P150; Platinum LED, Lights LLC, Kailua, HI) was adapted in a cooled light-reflecting PhotoQ Chamber (figure 1). We selected the LED lamp, because of its efficiency; low wattage, low energy consumption, low heat generation, and capacity for long duration and continuous use. The LED lamp has 50 diodes with a broad light spectrum including UV spectrum violet (360–400 nm), blue light (400–500 nm), and orange/red light (600–710 nm).

The PhotoQ apparatus (Figure 1) comprised the LED lamp and photoQ chamber; the light reflecting surface unit with the insulated floor (with the aid of Styrofoam), 2 ice packs, and 2 glass boxes of ice. Aluminum foil was used to laminate the walls and floor of the chamber to enhance the reflection of light onto the samples and conserve energy and increase efficiency. The ice packs served to lower the temperature of the PhotoQ chamber while the iceboxes maintained the cooling and reduced evaporation of the PBS solution in the samples during exposure for up to 72 h. With the icebox, there was no need to replenish the PBS solution in the samples for the period of PhotoQ. The ice also maintained the temperature at 25−26°C throughout the illumination period. The PhotoQ chamber was used in a cold room (4°C) for the entire LED exposure. Since the air temperature above the samples and the temperature at the sample surface are directly proportional to the distance of the lamp from the surface of the samples, we placed the lamp 10 cm above the samples to prevent overheating and to yield maximum light intensity exposure to the tissue. The LED lamp generates heat due to its limited efficiency in converting electrical energy into light (Duong and Han, 2013). NB: For the first set of exposure, we would advise the experimenters to monitor the photoQ chamber
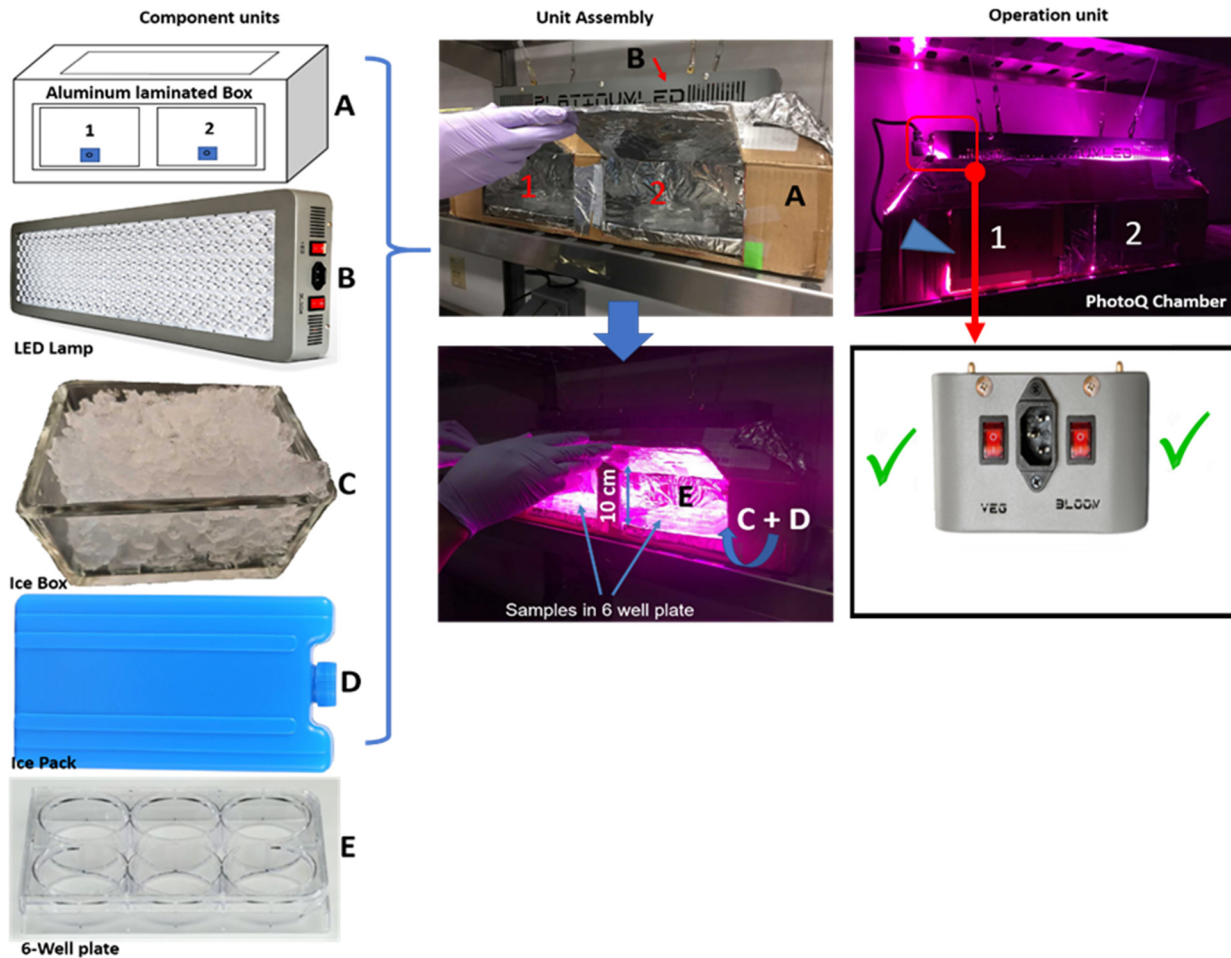
Figure 1. Photoq set-up showing the component units, unit assembly, and operation unit.
(A) Box laminated with the full aluminum interior. (B) 87-watt LED lamp with UV and infrared features for photoQ. (C) Glass box for ice (Ice-box) for cooling the photoQ chamber and reducing PBS evaporation in the samples. (D) Ice-pack for cooling the photoQ chamber and reducing PBS evaporation in the samples. (E) 6-well plate for sample collection and photoQ. (F) Both lamp switches are activated for the 87-watt lamp.

temperature and PBS evaporation rate for about 24 h to ensure the heat is at a moderate level.

Immunofluorescent Staining

After photoQ, tissue samples were immunolabelled using a rabbit anti-Iba1 antisera (Wako Chemical, Richmond, VA; 019-19741(RRID: AB_839504); 1:500) and a mouse anti-NeuN antibody (Millipore; MAB377 (RRID: AB_2298772); 1:500). Tissue samples were blocked in 5% normal goat serum (NGS) for an hour at room temperature with constant agitation and thereafter incubated in primary antibody overnight at 4°C with 5% NGS in PBS and 0.3% Triton with constant agitation. This was followed by 2 PBS washes of 5 min and subsequent incubation in the secondary antibodies in 5% NGS in PBS and 0.3% Triton with constant agitation at room temperature for an hour. The samples were then washed twice for 5 min each and mounted on slides in an aqueous mounting medium. To compare the effectiveness of our photoQ findings with a chemical quenching protocol before or after the IHC stains, the sections were washed for 3×10 min and immersed in TrueBlack® Lipofuscin Autofluorescence Quencher (Biotium Inc., CA, USA) for 30 s to reduce autofluorescence from lipofuscin and other sources as recommended by the manufacturer. Images were acquired (image stack of 31 μm thick and 1 μm dissector height) using a Nikon Eclipse Ti laser confocal microscope with pinhole (1.2), sensitivity (HV), laser power, and offset kept constant for all image acquisitions. The blue, green, and red channels were captured at 405 nm, 488 nm, and 561 nm excitation wavelengths.

CD44 Polymerase Chain Reaction (PCR)

We analyzed CD44 splice variant expression in samples of RNA isolated from each of five human cases, as previously described (van Weering et al., 1993). cDNA was synthesized using 500 ng
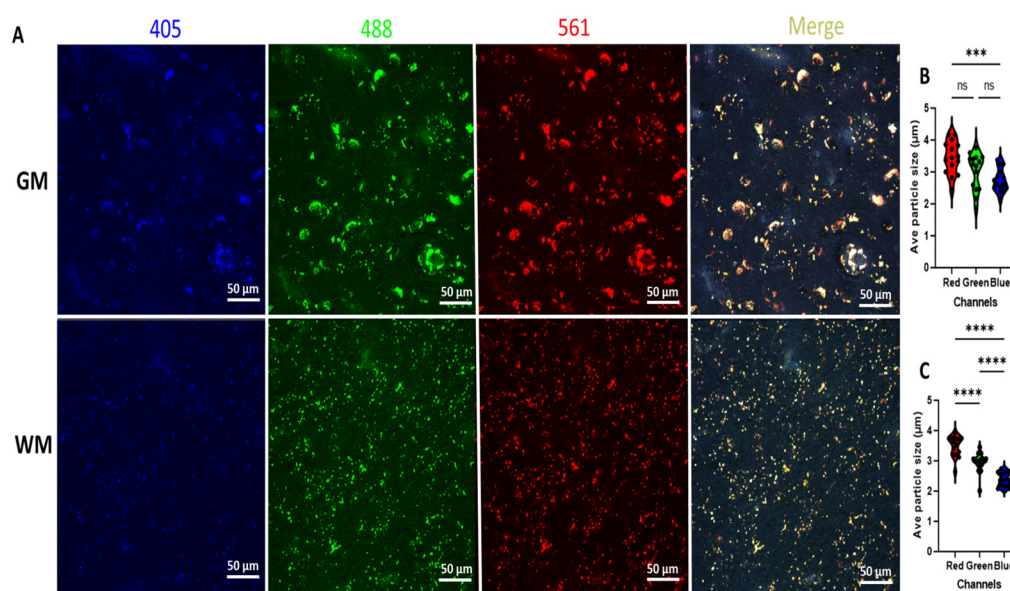
Figure 2. Photomicrographs from human brain (white and gray matter) before light exposure (nPhotoQ).
(A) Photomicrographs showing LAF fluorescence levels at 405, 488, and 561 nm wavelength in human white and gray matter before photo-quenching (nPhotoQ). (B) Violin plots showing the comparison of the average LAF particle size at 405, 488, and 561 nm wavelength in grey matter (GM) (***$p = 0.0006$, ns $p > 0.05$) (C) violin plots showing the comparison of average LAF particle size at 405, 488, and 561 nm wavelength in white matter (WM) (****$p < 0.0001$).

of RNA and primer C12AR: 5'-ATG CAA ACT GCA AGA ATC with Applied Biosystems™ High-Capacity cDNA Reverse Transcription Kit (Thermo-Scientific) in 20 ml. PCR reactions were run using Thermo Scientific™ Phusion™ High-Fidelity DNA Polymerase (Thermo-Scientific) at an annealing temperature of 56°C on a Bio-Rad C1000 Thermal Cycler, RRID: SCR_019688. For amplification of all CD44 variants, we used 40 ng of reverse transcriptase (RT) with the following primers: C2AR: 5'- CCA AGA TGA TCA GCC ATT CTG G and C13F: 5'- AAG ACA TCT ACC CCA GCA AC. For amplification of CD44 variants that included the V8 sequence, we used the primers PV8F: 5′-TCC AGT CAT AGT ACA ACG CT and C13F: 5′- AAG ACA TCT ACC CCA GCA AC with the following conditions: 1 ml of RT with GC buffer supplemented with 5 mM of Mg^{2+}, 200 mM dNTPs, 0.5 mM of each primer, and 0.02 U/mL of Phusion Hot start DNA Polymerase. Samples were then analyzed using standard gel electrophoresis protocols.

RNAscope® Protocol

Paraffin-embedded human brain sections were cut at 10 μm, with three consecutive tissue sections per sample. Sections were air-dried at room temperature (RT), submerged in 1X PBS, and exposed to the photoQ protocol (above). Probes targeting total CD44 (CD44v1; standard) and CD44v8 were detected using an RNAscope® Multiplex Fluorescent v2 Assay Kit (ACD Bio., Cat. #323100). Briefly, sections were deparaffinized, treated with hydrogen peroxide for 10 min at

RT, and washed twice in ddH$_2$O for 2 min. Slides were immersed in 1X RNAscope® Target Retrieval Reagent (boiling for 15 min) and washed for 15-s at RT in ddH$_2$O, followed by 3-min at RT in 100% ethanol. Slides were next treated with RNAscope® Protease Plus pretreatment (30-min at 40°C) and washed twice in ddH$_2$O. Slides were next immediately hybridized with either a CD44 variant target probe mix (~50 μL/tissue section, 1 μL CD44v1 probe per 50 μL of CD44v8 probe), or with RNAscope® positive control or negative control probes, and incubated in an oven for 2 h. at 40°C. One tissue section per slide was treated with the CD44 variant probe mixture, one with a positive control probe, and a third was treated with a negative control probe. The positive control probe targets a common housekeeping gene; the negative control probe targets a bacterial gene. Afterward, slides went through serial hybridization and signal amplification steps (RNAscope® Multiplex FL v2 Amp 1 for 30 min at 40°C, RNAscope® Multiplex FL v2 Amp 2 for 30 min at 40°C, RNAscope® Multiplex FL v2 Amp 3 for 15 min at 40°C); each step followed by washing twice with 1X RNAscope® Wash Buffer, 2 min at RT. Slides were next treated with RNAscope® Multiplex FL v2 HRP-C1 and RNAscope® Multiplex FL v2 HRP-C2, each at 15 min at 40°C to develop the HRP signals. The signals were visualized using Opal™ Dye fluorophores. The HRP-C1 channel and probe were assigned the Opal™ 520 fluorophore (1/300, Akoya Biosciences, Cat. #FP1487001KT). The HRP-C2 channel and probe were assigned the Opal™ 690 fluorophore (1/300, Akoya Biosciences, Cat. #FP1497001KT). Slides were
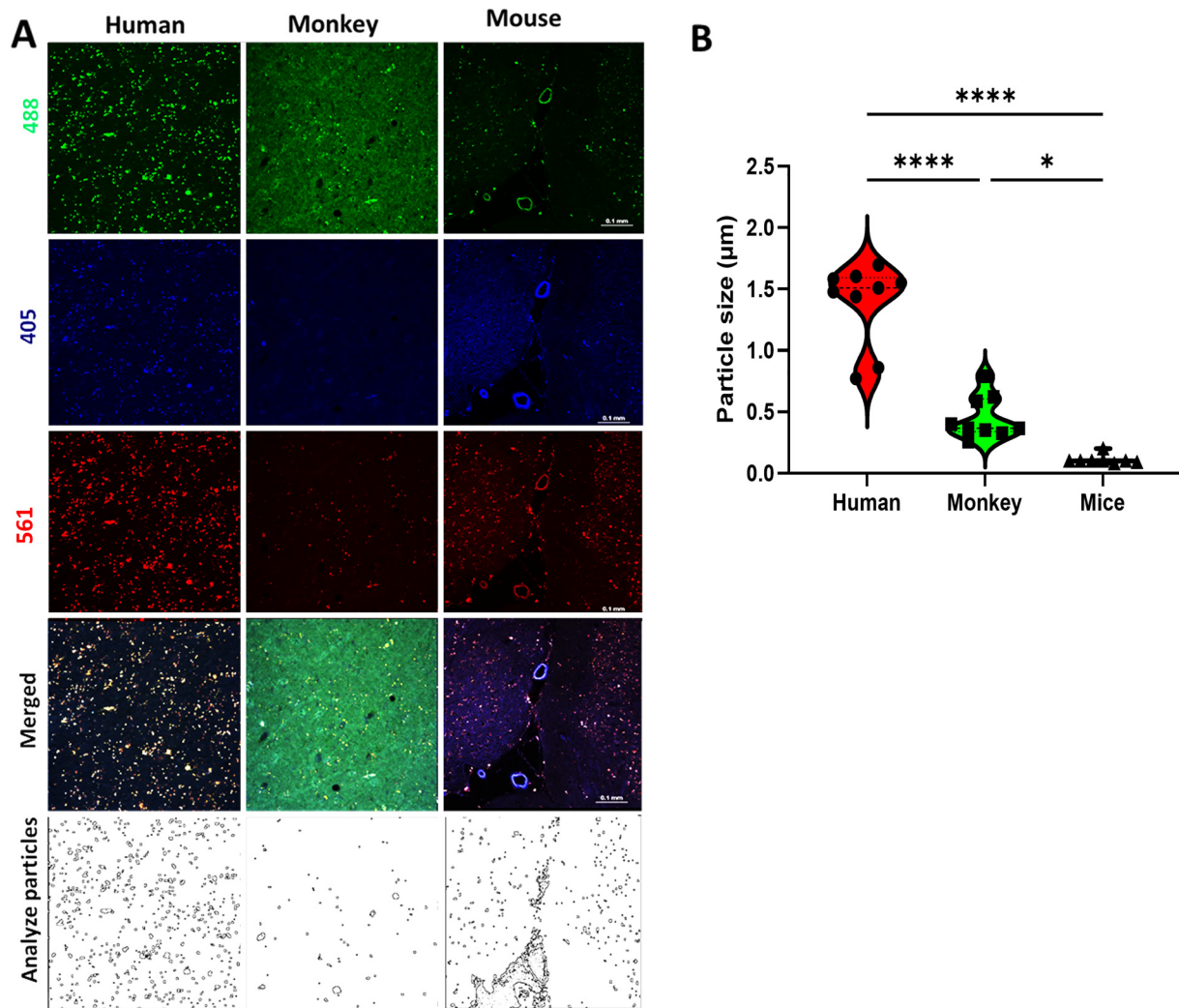
Figure 3. Photomicrographs from human, monkey, and mouse cerebral white matter before light exposure (nPhotoQ). (A) Photomicrographs showing LAF fluorescence level at 405, 488, and 561 nm wavelength in human, monkey, and mouse WM before photo-quenching (nPhotoQ). (B) Violin plots showing the average LAF particle size across all three species (****p < 0.0001, *p = 0.0116). Lower panels show the typical distributions of particles and sizes in the white matter from the three species.

treated with fluorophores for 30 min at 40°C, followed by two washes in 1X RNAscope® Wash Buffer for 2 min at RT. Slides were mounted in ProLong™ Diamond Antifade Mountant with DAPI (Invitrogen, Cat. #P36971) and stored at 4°C in the dark. Slides were visualized with Zeiss Axio Imager M2 apotome microscopy with Stereo Investigator® software (MBF Bioscience).

Statistical Analysis

Data are expressed as mean $\pm$ standard error of mean (SEM). The statistical significance was determined using two–way ANOVA analysis and Tukey's multiple mean comparisons of fluorescence Intensity [I], percentage reduction for the treated duration [II], and LAF particle size. Probability values of <0.05 were considered to represent statistically

significant differences. Statistical analysis was conducted using GraphPad Prism Software (GraphPad Software Inc., La Jolla, CA).

Results

Lipofuscin autofluorescence (LAF) level and particle size in humans, monkeys, and mice. Although brain tissue levels of lipofuscin (LAF) accumulate with aging, there is little information on the relative LAF particle sizes and fluorescence levels in human, macaque, and mouse gray matter (GM) or white matter (WM). Consistent with prior observations, we found that LAF particles in aging human GM and WM were numerous, intensely fluorescent, and ranged in size from about 2−5 µm (Figure 2). The LAF in GM was more dispersed and appeared larger compared to that in
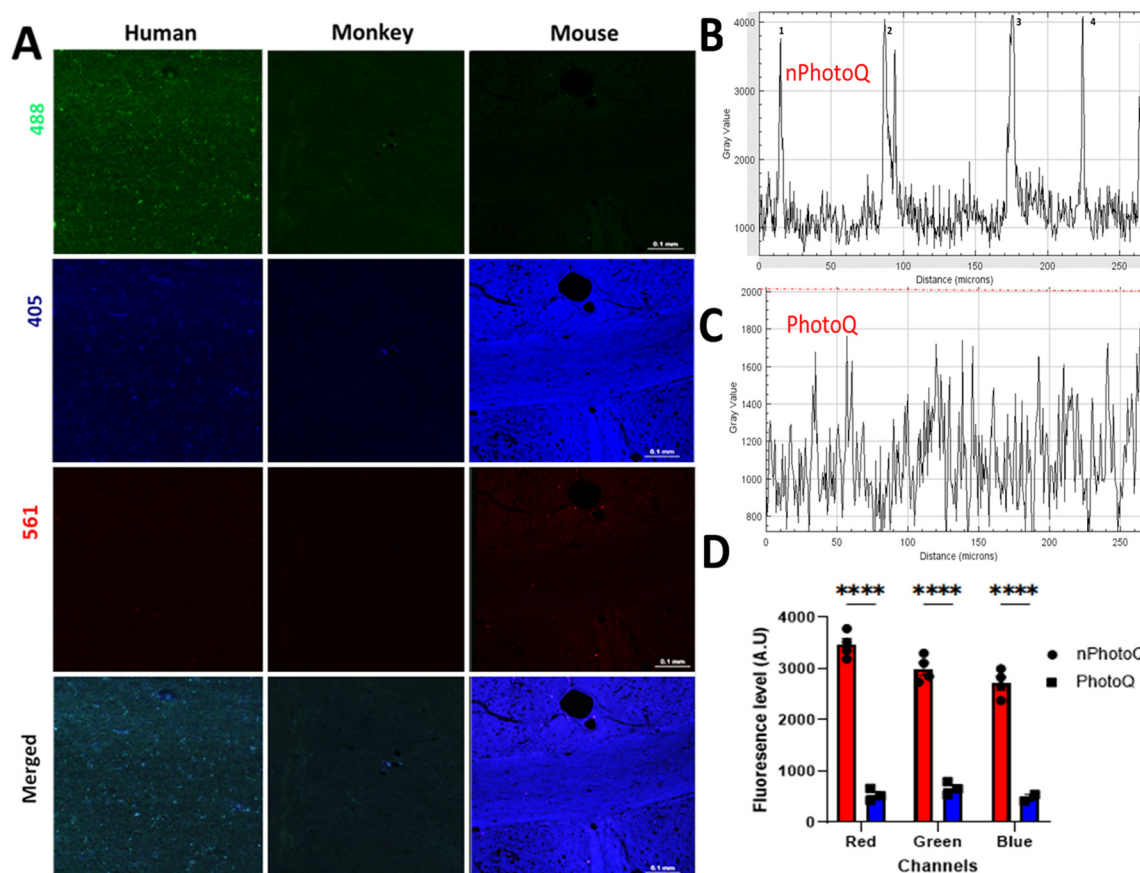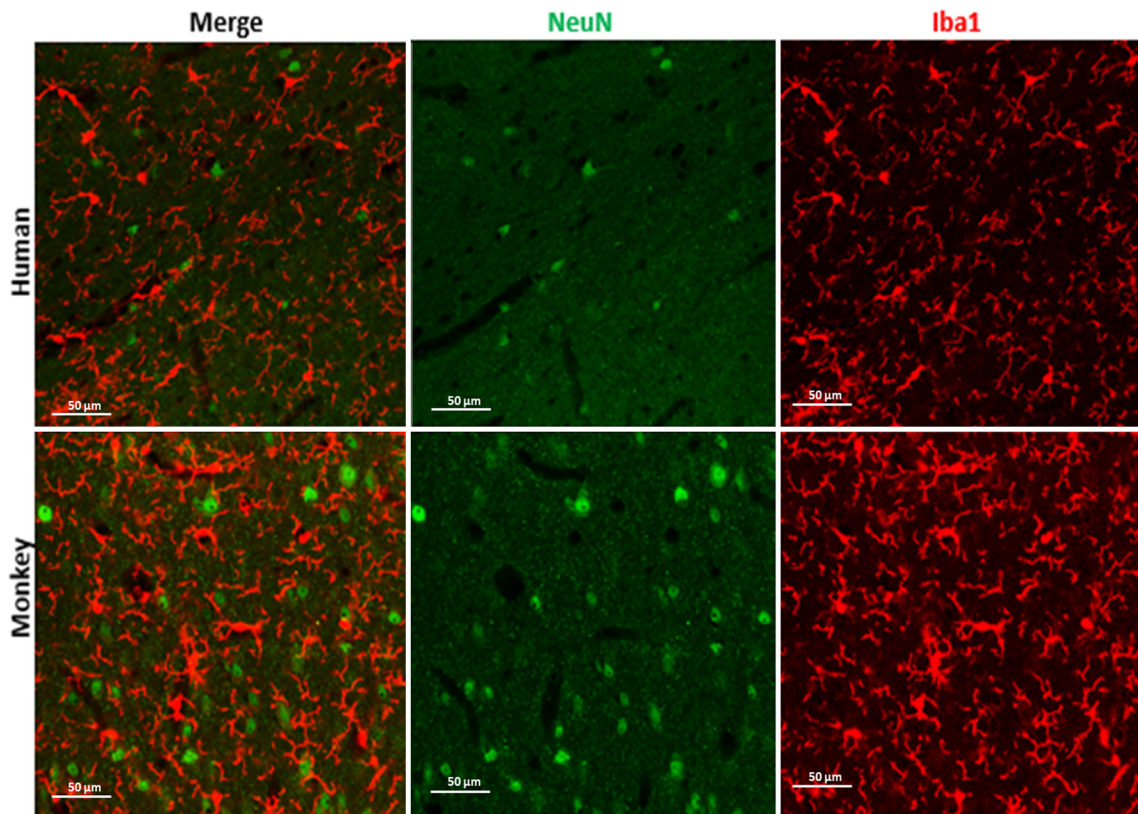
Figure 4. Photomicrographs from human, monkey, and mouse cerebral white matter after 72 h light exposure.
(A) Photomicrographs showing fluorescence levels at 405, 488, and 561 nm wavelength in human, monkey, and mouse WM. (B) Gray value graph showing the LAF fluoresce intensity level and background in a human WM sample before photoQ exposure with high peaks (1, 2, 3,4, and 5). (C) Gray value graph showing the reduced fluorescence intensity levels and background after 72 h photoQ exposure from the same human WM sample as in B. (D) Bar graph showing the comparison of fluorescence levels before and after the light exposure (****p < 0.0001) in a human sample using the approach illustrated in supplemental figure 1.

WM (Fig. 2A). There was no significant difference in the LAF average particle size in human GM when compared with WM (red: p = 0.9997, green: p = 0.09951, blue: p = 0.2201; Fig. 2B and C). Average LAF particle size is higher in the green/red channels compared to the blue channel both in GM (p < 0.001) and WM (p < 0.0001, Fig. 2B and C).

We next determined the optimal duration of mLED exposure (12, 24, 48, 72, or 100 h) that near eliminated LAF when temperature and mLED lamp level (distance from the lamp surface to the sample) were held constant. We found that maximal LAF quenching was achieved within 72-h for all the species evaluated (Supplemental Figure 2 and data not shown). To determine the magnitude of LAF reduction after photoQ, we first quantified basal levels of LAF fluorescence in aging GM and WM relative to the tissue background fluorescence in humans, macaque, and mice (Fig. 2A to C). Figure 3A shows the typical appearance of LAF as visualized at peak emission at 488 nm, 405 nm, and 561 nm in humans, monkeys, and mice. As described in the methods, we

estimated the magnitude of LAF emission for humans, mice, and macaques at 405 nm, 488 nm, and 561 nm and report these as individual values (Table 1). Fluorescence values for human [2717.3 ± 95.4 (red), 2999.8 ± 108.9 (green), and 3460.3 ± 97.7 (blue)] and macaque [2051.5 ± 210.4 (red), 2693.2 ± 289.8 (green), and 3082.2 ± 215.6 (blue)], were markedly higher than for mouse [66.1 ± 2.4 (red), 45.6 ± 3.2 (green), and 49.2 ± 5.6 (blue)]. As shown in Figure 3A, there was no apparent difference in LAF levels between red and green channels in humans and monkeys while the LAF level in the blue channel was less prominent. We estimated the LAF average particle size in human WM (Fig. 3B) and found it to be significantly larger than in macaque (p < 0.0001) or mouse (p < 0.0001). Similarly, the LAF average particle size in macaque was significantly larger than in mouse (Fig. 3B; p = 0.0116).

PhotoQ elimination of lipofuscin autofluorescence (LAF) for fluorescence multi-labeling. We next quantified the magnitude of photo quenching of LAF after 72-h exposure

Figure 5. Photomicrographs of NeuN and Iba1 stain from human and monkey cerebral white matter after 72 h photoQ exposure. Scale bar: 50 μm.

to light. When compared to Fig. 3A and Table 1, there was a pronounced reduction in LAF in humans, monkeys, and mice (Fig. 4A; Supplemental Figure 3). In all three species, the LAF level was effectively reduced from an average of 4200 AU to an average of 800 AU gray value (Fig. 4B to D; p < 0.0001) in all three channels. The tissue background before (1500 AU) and after (1250 AU) mLEDs exposure was similar (Fig. 4B, C; Supplemental Figure 1) in all three channels. The pronounced reduction in LAF intensity can be appreciated from typical plots of fluorescence intensity values before (Fig. 4B) and after photoQ (Fig. 4C), as derived from scans across human WM tissue samples. Figure 4D shows a plot of the LAF levels before and after photoQ in a human WM sample, which demonstrates the significant reduction in LAF that was typically observed (****p < 0.0001). We estimated that photoQ reduced the mean LAF from all three channels by $94.5 \pm 0.96\%$ (n = 5 cases). This pronounced level of reduction in LAF made it feasible to routinely visualize multiple antigens by fluorescence immunohistochemistry. Figures 5 and 6, and S3 demonstrate that after 72 h photo quenching, it was feasible, for example, to co-visualize microglia labeled with Iba1 (red) and neuronal nuclei labeled with NeuN (green) in the same tissue section. Whereas specific IHC staining for NeuN and Iba1

was not identified with true black (TB) treatments (Figure 6), photoQ permitted specific detection of both antigens.

Fluorescence CD44 variant detection in aging human white matter. The CD44 transmembrane glycoprotein has been implicated in neuroinflammatory and neurodegenerative diseases and brain aging in humans (Peters and Sherman, 2020). The human *CD44* gene includes 9 variant exons (v2-v10) that generate alternative RNA splice variants encoding diverse CD44 proteins. We examined the expression of splice variant 8 (CD44v8) of CD44 expressed in the brains of five human cases (Supplemental Table 1). We focused on CD44v8 because CD44v8 containing splice variants have been implicated in endothelial junction disruption (Zhang et al., 2014). Notably, aging-associated white matter injury has been shown to display blood-brain barrier disruption related to microvascular ischemia (Hussain et al., 2021).

In addition to a 'standard' form of CD44 (CD44s) that lacks variant exon-encoded sequences (Fig. 7), weakly amplified higher-sized bands were observed following PCR reactions using primers that are common to all forms of CD44 (Fig. 7A). We then performed additional PCR reactions for each of the variants and found that these tissues express multiple splice variants, including variants carrying v8 sequences (Fig. 7B and data not shown).
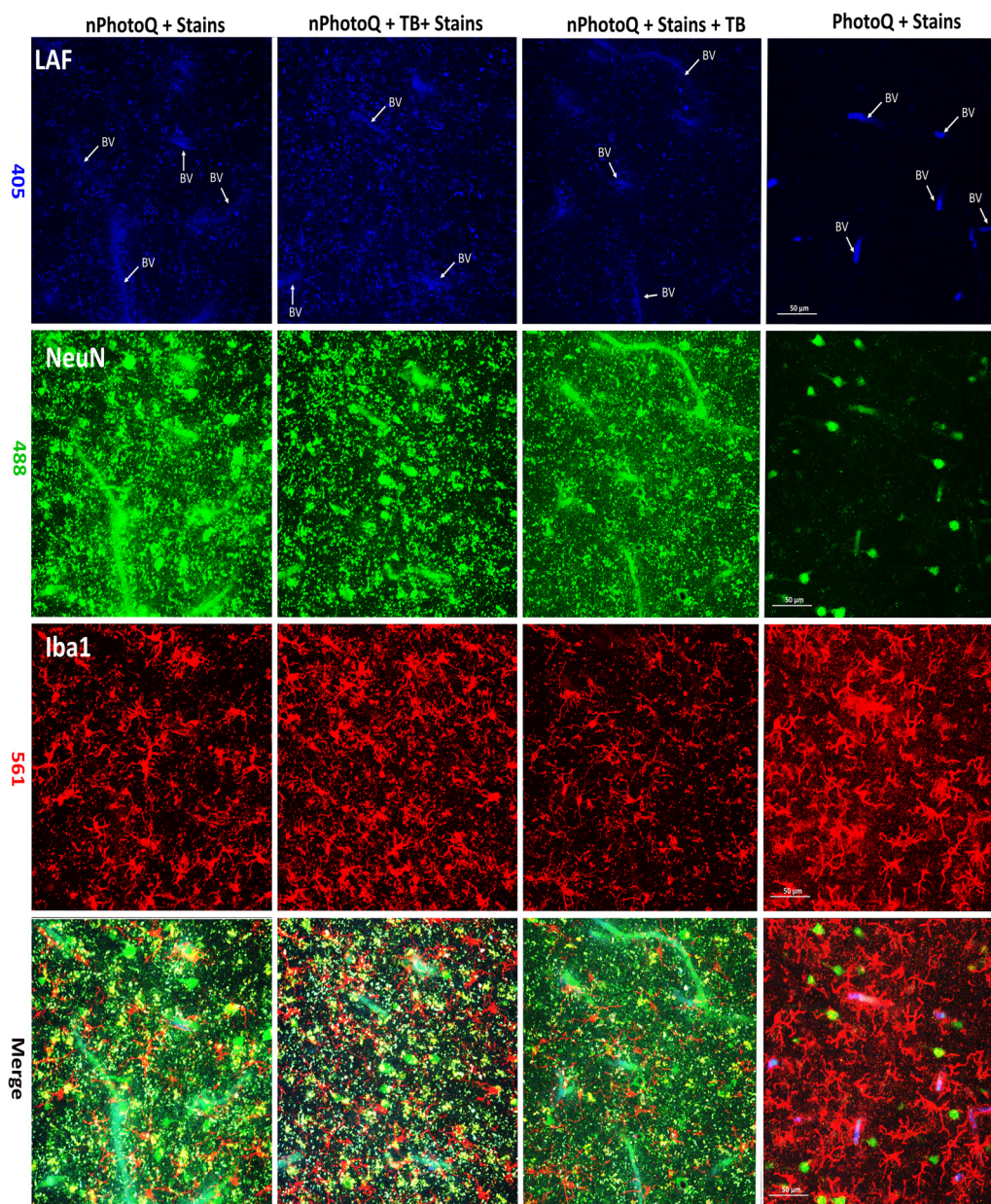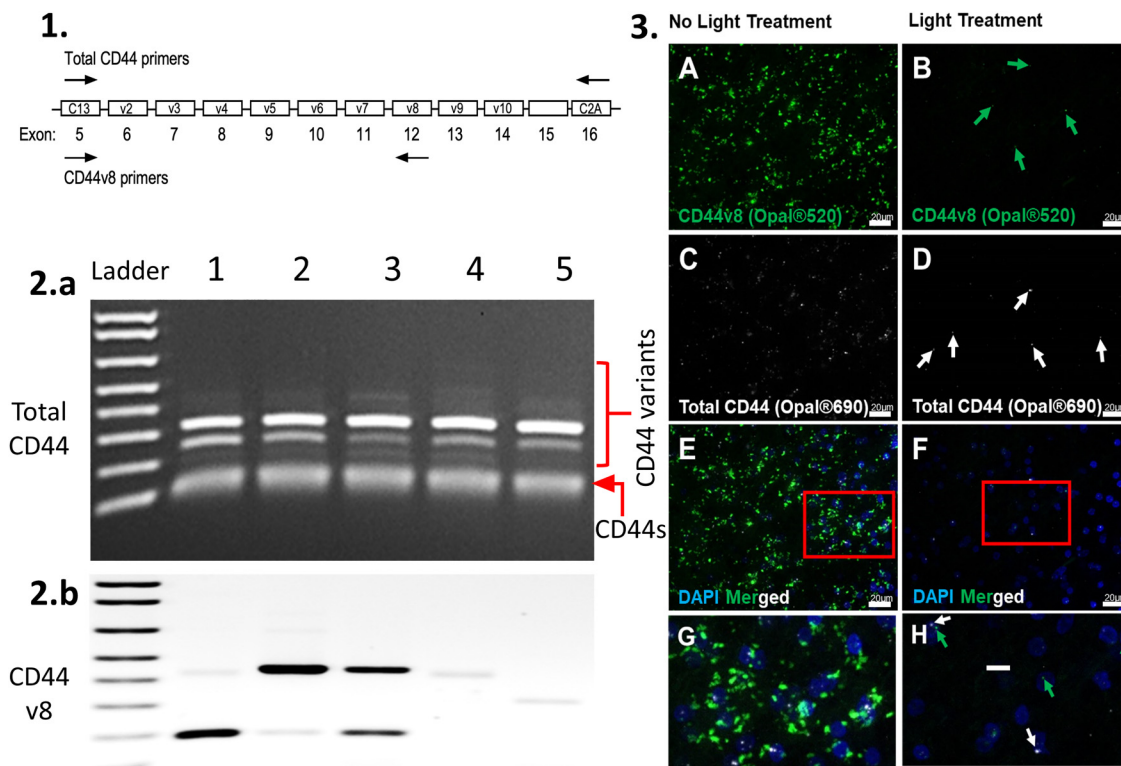
Figure 6. Photomicrographs of human cerebral white matter demonstrate LAF with or without treatment with trueBlack® (tb) or photoQ. Panels imaged at 405 nm: unstained to visualize only LAF (Blue). Panels imaged at 488 nm: NeuN (Green). Panels imaged at 561 nm: Iba1 (Red) Merge is shown in lower panels. Key to staining conditions: **nPhotoQ + Stains**: no photoQ with stains; **nPhotoQ + TB + Stains**: no photoQ with TrueBlack® followed by IHC; **nPhotoQ + Stains + TB**: no photoQ with IHC followed by TrueBlack®; and **PhotoQ + stains**: section treated with PhotoQ follow by IHC. **BV**: Blood vessel. Scale bar: 50 μm.

To further validate our photo quenching protocol, we also evaluated LAF elimination by photoQ treatment using an RNAscope fluorescence in situ hybridization technique in aging human cerebral white matter. Commercially available probes for total CD44 and CD44v8 were obtained and employed on human brain samples (Figure 7A to H). After light treatment, the total CD44 and CD44v8 probes were readily detected in human cerebral white matter (Figure 7). The enhanced detection of the total CD44 and CD44v8 puncta was achieved after LAF

elimination, while in the non-photoQ slides, many of the puncta could not be differentiated from the LAF signal (Figure 7B, D, F, and H), rendering this technique unusable in non-photoQ tissue (Figure 7A, C, E, and G).

Discussion

The progressive accumulation of lipofuscin and other autofluorescent compounds in the aging brain has been a significant

Figure 7. Schematic showing total CD44 primers (**1**), blot total CD44 (**2. a:** CD44s + CD44 variants), and variant 8 (**2. b:** CD44 v8) from five human cerebral white matter samples. Photomicrographs of RNAscope® processed human tissue with (**3:** B, D, F, and H) or without (**3:** A, C, E, and G) photoQ. The Hs-CD44-C2 probe detects Homo sapiens CD44 molecule (Indian blood group) (CD44) transcript variant 1 mRNA, containing all variant exons, and the Hs-CD44-O1 probe detects Homo sapiens CD44 molecule (Indian blood group) (CD44) transcript variant 8 mRNA. Scale bar: 20 μm (G and H).

impediment to successfully employing fluorescence-based histological approaches to study mechanisms of neurodegeneration. We report here that exposure to high-intensity multispectral light-emitting diodes (mLEDs) is a simple, cost-effective means to eliminate LAF in aging brain tissue of varying thicknesses (20 −50 μm) from humans, macaques, and mice. The protocol we developed is feasible with both free-floating and glass slide-mounted tissue sections (cryostat cut or paraffin-embedded) and can be adapted to efficiently process multiple samples to ensure high throughput and reproducibility. Importantly, our 72-h photo-quenching protocol did not affect tissue integrity or the quality of fluorescent immunohistochemical staining (see Figs. 5 and 6) or in situ hybridization (see Fig. 7) compared to untreated sections. Moreover, the elimination of LAF appeared to be irreversible, even in tissue sections stored for a year after photo-quenching (data not shown). We estimate that LAF was reduced by $95 \pm 1\%$ by our 72-h photo-quenching protocol. Essentially complete elimination of LAF was achieved with a 100-h photo-quenching protocol. However, we found that 72 h was sufficient to confidently distinguish specific immunostaining from LAF in all three species tested. However, the duration of photo-quenching may vary for different tissue applications and may need to be adjusted to optimize the protocol. One important consideration is access to a cooling apparatus to mitigate the

excessive heat generation involved with prolonged exposure to mLEDs. Placement of the mLED arrays in a cold room together with additional ice trays and cold packs prevented excessive heat generation by the mLEDs and excessive evaporation of staining solutions. We typically found that with these cooling measures, the interior of the chamber was maintained at about 25°C throughout the 72-h photoQ protocol. A limitation of the protocol is that we did not specifically test the degree of quenching achieved for hemosiderin or other blood products, which were not detected in our samples. Moreover, our protocol did not reduce blood vessel-associated autofluorescence to the same magnitude as achieved with LAF (see Fig. 6).

We initially tested lower-intensity LED arrays (Duong and Han, 2013; Sun et al., 2017), but found that quenching of LAF was incomplete for human brain tissue from advanced aging, where lipofuscin pigments were extremely high. A prior study found LED arrays to be effective for reduction of autofluorescence in cat and rabbit brain tissue but did not evaluate aging human or nonhuman primate brain tissues, which are highly enriched in intensely fluorescent lipofuscin pigments (Duong and Han, 2013). In agreement with these prior studies, we also found that photoQ did not compromise the staining of nuclear (NeuN) or cytoplasmic (Iba1) antigens as well as other markers (see Figs. 5 and 6), which included

membrane-associated markers (CD44) and oligodendrocyte lineage markers (platelet-derived growth factor receptor alpha) and myelin basic protein (data not shown). This contrasts with chemical quenching agents, which were not effective in significantly reducing LAF in the aging brain and reduced specific immunofluorescent staining (see figures 6 and Supplemental S3).

Despite the extensive use of mouse models in aging studies, the impact of LAF on the histological analysis of these models has not been systematically addressed in cerebral white matter. Although mice appear to differ from higher mammals in the ultrastructural features of CNS (Central Nervous System) lipofuscin (Samorajski et al., 1965; Boellaard et al., 2004), species-specific differences in the accumulation of lipofuscin in aging brain have not been defined. Although we found quantitatively lower levels of LAF fluorescence and particle sizes (Fig. 3) in aging mice compared to humans and macaque, the levels were nevertheless sufficient to confound the interpretation of immunostaining results. Although our results are limited by the low number of aging mice, which were available for study, they support that the accumulation of LAF appears to broadly occur in the brain of aging mammals, including rodents, and unless quenched, has the potential to contribute to spurious results in mouse models, as well as humans.

Our analysis of novel CD44 variant expression in aging-associated human cerebral white matter lesions demonstrates that LAF posed significant challenges to validate our results. Although CD44 contributes to inflammatory-mediated responses to cerebral injury (Peters and Sherman, 2020) as well as CNS tumor progression (Nagasaka et al., 1995; Jijiwa et al., 2011), the role of CD44 variants in the response to human white matter injury has not been defined. Alternative RNA splicing generates multiple CD44 variants, which involves nine exons in humans (Chen et al., 2018). In addition to the standard form of CD44 (CD44s), multiple CD44 variants exist in the normal human brain (Kaaijk et al., 1997). Whereas some CD44 variants are enriched in neuritic plaques and astrocytes, variants 3, 6, and 10 are neuronally associated in the human hippocampus with Alzheimer's disease pathology (Pinner et al., 2017). We previously reported that astrocyte-enriched CD44 is elevated both in human neonatal white matter injury (Buser et al., 2012) and in gray matter from nonhuman primates with normative aging (Cargill et al., 2012). Hyaluronan is one of the principal endogenous ligands for CD44 and is enriched in frontal cerebral white matter lesions in cases of vascular dementia (Back et al., 2011).

We chose to detect CD44 variants by in situ hybridization to determine if our photoQ protocol is compatible with more complex fluorescence detection techniques in addition to immunohistochemistry. Since our RNAscope detection protocol utilized paraffin-embedded tissue sections, this allowed us to confirm that photo-bleaching was compatible with this form of archival tissue preservation, which is typically employed in human neuropathological studies. Moreover,

an *in-situ* approach allowed us to validate findings from PCR variant detection. Indeed, although the standard form of CD44 was detected in all five cases by PCR, the CD44v8 splice variant displayed different expression patterns in each case (Fig. 7). Hence, we employed a complementary strategy to detect total CD44 vs. CD44v8 in situ by RNAscope. Without photo-bleaching, the diffuse distribution and high levels of LAF obscured specific fluorescent signals from the total CD44 and CD44v8 RNAscope probes. We also found that the size of the probe label was very similar to smaller LAF particles, which confounded the specific identification of both the total CD44 and CD44v8 probes. The application of the PhotoQ protocol allowed us to specifically distinguish the relative cellular distribution of total CD44 and CD44v8 and to validate results from PCR-based analyses of CD44 splice variants. Our findings thus suggest a potential role for CD44v8 in vascular disruption in aging human white matter, since the CD44v8 containing splice variant has been previously implicated in endothelial junction disruption (Hussain et al., 2021). Our limited analysis of five white matter injury cases included cases with pathological Alzheimer's disease and/or vascular brain injury (Supplementary Table 1). Endothelial disruption related to blood-brain barrier disruption has been described both for Alzheimer's disease and for vascular brain injury (Hussain et al., 2021). Larger numbers of human white matter injury samples will be needed to confirm the potential roles of CD44v8 in aging white matter.

In summary, we have addressed the unique technical challenges that LAF poses to studying mechanisms of neurodegeneration in the aging brains of humans, nonhuman primates, and mice. We have validated a simple, cost-effective protocol using high-intensity mLEDs to eliminate lipofuscin autofluorescence in aging brain tissue, which constitutes a major impediment to the specific detection of fluorescently tagged markers employed in immunohistochemistry and in situ hybridization. We hope that this protocol can be widely adapted to accelerate progress in aging research.

Author Contributions

P.A.A. conceptualized the project. P.A.A., Z.B., L.S.S., C.D.K., and S.A.B. were responsible for the study design. P.A.A., S.A.B., K.F., Z.B., and L.S.S., wrote, edited, and finalized the manuscript. C.D.K. supervised all human pathology studies. P.A.A., X.G, and M.G. conducted histological studies. K.A.F. conducted RNAscope studies. F.B. conducted molecular CD44 variant studies.

Data Availability

We declare that the data supporting the findings of this study are available within the article and its supplementary information files and from the corresponding authors upon request.

Abbreviations

AD   Alzheimer's disease (Braak's score ≥ 3)

CD44	Cluster of Differentiation 44
CD44s	Standard form of Cluster of Differentiation 44
CMI	Cerebromicrovascualr injury
GM	Grey matter
IHCI	Immunohistochemistry
LAF	lipofuscin-associated autofluorescence
LED	Light Emitting Diodes
MINS	Minutes
mLEDs	Multispectral light-emitting diodes
nAD	no Alzheimer's disease (Braak's score <3)
nCMI	no Cerebromicrovascualr injury
PCR	Polymerase Chain Reaction
PhotoQ	Photo Quenching/ bleaching
PMI	Post-mortem interval
SEM	Standard Error of Mean
UV	Ultraviolet
WM	White matter
WT	Wide type
x	mean

ORCID iD

Philip A. Adeniyi ⬢ https://orcid.org/0000-0001-7800-6937

Summary Statement

We addressed the unique technical challenges to study mechanisms of white matter injury in the aging brain using fluorescent immunohistochemistry and RNAscope® in situ hybridization. We developed a cost-effective photobleaching protocol that essentially permanently eliminates most autofluorescence in the aging brain.

Acknowledgments

Declaration of Conflicting Interests

Funding

Supplemental Material

Supplemental material for this article is available online.

References

Andrews, L. D., & Brizzee, K. R. (1986). Lipofuscin in retinal pigment epithelium of rhesus monkey: Lack of diminution with centrophenoxine treatment. *Neurobiology of Aging*, *7*(2), 107–113. https://doi.org/10.1016/0197-4580(86)90148-x

Back, S. A., Kroenke, C. D., Sherman, L. S., Lawrence, G., Gong, X., Taber, E. N., Sonnen, J. A., Larson, E. B., & Montine, T. J. (2011). White matter lesions defined by diffusion tensor imaging in older adults. *Annals of Neurology*, *70*(3), 465–476. doi:10.1002/ana.22484

Baharlou, H., Canete, N. P., Bertram, K. M., Sandgren, K. J., Cunningham, A. L., Harman, A. N., & Patrick, E. (2021). AFid: A tool for automated identification and exclusion of autofluorescent objects from microscopy images. *Bioinformatics (Oxford, England)*, *37*, 559–567. doi:10.1093/bioinformatics/btaa780

Banerjee, B., Miedema, B. E., & Chandrasekhar, H. R. (1999). Role of basement membrane collagen and elastin in the autofluorescence spectra of the colon. *Journal of Investigative Medicine*, *47*(6), 326–332. https://doi.org/10.1093/bioinformatics/btaa780

Boellaard, J. W., Schlote, W., & Hofer, W. (2004). Species-specific ultrastructure of neuronal lipofuscin in hippocampus and neocortex of subhuman mammals and humans. *Ultrastructural Pathology*, *28*, 341–351. doi:10.1080/019131290882330

Brizzee, K. R., Cancilla, P. A., Sherwood, N., & Timiras, P. S. (1969). The amount and distribution of pigments in neurons and glia of the cerebral cortex. Autofluorescent and ultrastructural studies. *Journal of Gerontology*, *24*, 127–135. doi:10.1093/geronj/24.2.127

Brizzee, K. R., & Johnson, F. A. (1970). Depth distribution of lipofuscin pigment in cerebral cortex of albino rat. *Acta Neuropathologica*, *16*, 205–219. doi:10.1007/BF00687360

Buser, J., Maire, J., Riddle, A., Gong, X., Nguyen, T., Nelson, K., Luo, N., Ren, J., Struve, J., Sherman, L., Miller, S., Chau, V., Hendson, G., Ballabh, P., Grafe, M., & Back, S. (2012). Arrested preoligodendrocyte maturation contributes to myelination failure in premature infants. *Annals of Neurology*, *71*, 93–109. doi:10.1002/ana.22627

Cargill, R., Kohama, S. G., Struve, J., Su, W., Banine, F., Witkowski, E., Back, S. A., & Sherman, L. S. (2012). Astrocytes in aged nonhuman primate brain gray matter synthesize excess hyaluronan. *Neurobiology Of Aging*, *33*(830), e813–e824. doi: 10.1016/j.neurobiolaging.2011.07.006.

Chen, C., Zhao, S., Karnad, A., & Freeman, J. W. (2018). The biology and role of CD44 in cancer progression: Therapeutic implications. *Journal of Hematology & Oncology*, *11*, 64. doi:10.1186/s13045-018-0605-5

Corrêa, F. M., Innis, R. B., Rouot, B., Pasternak, G. W., & Snyder, S. H. (1980). Fluorescent probes of alpha- and beta-adrenergic and opiate receptors: Biochemical and histochemical evaluation. *Neuroscience Letters*, *16*, 47–53. doi:10.1016/0304-3940(80)90099-3

Duong, H., & Han, M. (2013). A multispectral LED array for the reduction of background autofluorescence in brain tissue. *Journal of Neuroscience Methods*, *220*, 46–54. doi:10.1016/j.jneumeth.2013.08.018

Hussain, B., Fang, C., & Chang, J. (2021). Blood-Brain barrier breakdown: An emerging biomarker of cognitive impairment in normal aging and dementia. *Frontiers in Neuroscience*, *15*, 688090. doi:10.3389/fnins.2021.688090

Jijiwa, M., Demir, H., Gupta, S., Leung, C., Joshi, K., Orozco, N., Huang, T., Yildiz, V. O., Shibahara, I., de Jesus, J. A., Yong, W. H., Mischel, P. S., Fernandez, S., Kornblum, H. I., & Nakano, I. (2011). CD44v6 Regulates growth of brain tumor stem cells partially through the AKT-mediated pathway. *PLoS One*, *6*, e24217. doi:10.1371/journal.pone.0024217

Kaaijk, P., Pals, S. T., Morsink, F., Bosch, D. A., & Troost, D. (1997). Differential expression of CD44 splice variants in the normal human central nervous system. *Journal Of Neuroimmunology*, *73*, 70–76. doi:10.1016/S0165-5728(96)00167-1

Leavesley, S. J., Annamdevula, N., Boni, J., Stocker, S., Grant, K., Troyanovsky, B., Rich, T. C., & Alvarez, D. F. (2012). Hyperspectral imaging microscopy for identification and quantitative analysis of fluorescently-labeled cells in highly autofluorescent tissue. *Journal of Biophotonics*, *5*, 67–84. doi:10.1002/jbio.201100066

Moreno-García, A., Kun, A., Calero, O., Medina, M., & Calero, M. (2018). An overview of the role of lipofuscin in age-related neurodegeneration. *Frontiers in Neuroscience*, *12*, 464. doi:10.3389/fnins.2018.00464

Nagasaka, S., Tanabe, K. K., Bruner, J. M., Saya, H., Sawaya, R. E., & Morrison, R. S. (1995). Alternative RNA splicing of the hyaluronic acid receptor CD44 in the normal human brain and in brain tumors. *Journal of Neurosurgery*, *82*, 858–863. doi:10.3171/jns.1995.82.5.0858

Pang, Z., Barash, E., Santamaria-Pang, A., Sevinsky, C., Li, Q., & Ginty, F. (2013). Autofluorescence removal using a customized filter set. *Microscopy Research and Technique*, *76*, 1007–1015. doi:10.1002/jemt.22261

Peters, A., & Sherman, L. S. (2020). Diverse Roles for Hyaluronan and Hyaluronan Receptors in the Developing and Adult Nervous System. *International Journal Of Molecular Sciences*, *21*(17). 5988. doi: 10.3390/ijms21175988

Pinner, E., Gruper, Y., Ben Zimra, M., Kristt, D., Laudon, M., Naor, D., & Zisapel, N. (2017). CD44 Splice variants as potential players in Alzheimer's disease pathology. *Journal of Alzheimer's Disease : JAD*, *58*, 1137–1149. doi: 10.3233/JAD-161245

Samorajski, T., Ordy, J. M., & Keefe, J. R. (1965). The fine structure of lipofuscin age pigment in the nervous system of aged mice. *Journal of Cell Biology*, *26*, 779–795. doi:10.1083/jcb.26.3.779

Santer, R. M., Partanen, M., & Hervonen, A. (1980). Glyoxylic acid fluorescence and ultrastructural studies of neurones in the coeliac-superior mesenteric ganglion of the aged rat. *Cell and Tissue Research*, *211*, 475–485. doi:10.1007/BF00234401

Schnell, S. A., Staines, W. A., & Wessendorf, M. W. (1999). Reduction of lipofuscin-like autofluorescence in fluorescently labeled tissue. *Journal of Histochemistry and Cytochemistry*, *47*, 719–730. doi:10.1177/002215549904700601

Sun, Y., Ip, P., & Chakrabartty, A. (2017). Simple Elimination of Background Fluorescence in Formalin-Fixed Human Brain Tissue for Immunofluorescence Microscopy. *Journal of Visualized Experiments: JoVE*, *2017 Sep 3;*(2127), 56188. doi: 10.3791/56188.

Terman, A., & Brunk, U. T. (2004a). Lipofuscin. *International Journal of Biochemistry & Cell Biology*, *36*, 1400–1404. doi:10.1016/j.biocel.2003.08.009

Terman, A., & Brunk, U. T. (2004b). Myocyte aging and mitochondrial turnover. *Experimental Gerontology*, *39*, 701–705. doi:10.1016/j.exger.2004.01.005

van Weering, D. H., Baas, P. D., & Bos, J. L. (1993). A PCR-based method for the analysis of human CD44 splice products. *PCR Methods and Applications*, *3*, 100–106. doi:10.1101/gr.3.2.100

Viegas, M. S., Martins, T. C.,, Seco, F., & do Carmo, A (2007) An improved and cost-effective methodology for the reduction of autofluorescence in direct immunofluorescence studies on formalin-fixed paraffin-embedded tissues. *European Journal of Histochemistry*, *51*, 59–66.

Whittington, N. C., & Wray, S. (2017). Suppression of red blood cell autofluorescence for immunocytochemistry on fixed embryonic mouse tissue. *Current Protocols in Neuroscience / Editorial Board, Jacqueline N. Crawley. [et Al]*, *81*, 2.28.1–2.28.12. doi: 10.1002/cpns.35.

Woolfe, F., Gerdes, M., Bello, M., Tao, X., & Can, A. (2011). Autofluorescence removal by non-negative matrix factorization. *IEEE Transactions on Image Processing: A Publication of the IEEE Signal Processing Society*, *20*, 1085–1093. doi:10.1109/TIP.2010.2079810

Zhang, P., Fu, C., Bai, H., Song, E., Dong, C., & Song, Y. (2014). CD44 Variant, but not standard CD44 isoforms, mediate disassembly of endothelial VE-cadherin junction on metastatic melanoma cells. *FEBS Letters*, *588*, 4573–4582. doi:10.1016/j.febslet.2014.10.027